



Article

Underlying Mechanisms of Reductive Amination on Pd-Catalysts: The Unique Role of Hydroxyl Group in Generating Sterically Hindered Amine

Zeng Hong ^{1,2} , Xin Ge ^{3,*} and Shaodong Zhou ^{1,2,*}

¹ Zhejiang Provincial Key Laboratory of Advanced Chemical Engineering Manufacture Technology, College of Chemical and Biological Engineering, Zhejiang University, Hangzhou 310027, China; 12128008@zju.edu.cn

² Institute of Zhejiang University—Quzhou, 78 Jiu Hua Boulevard North, Quzhou 324000, China

³ School of Chemical and Material Engineering, Jiangnan University, Lihu Avenue 1800, Wuxi 214122, China

* Correspondence: gexin@jiangnan.edu.cn (X.G.); szhou@zju.edu.cn (S.Z.)

Abstract: Pd nanospecies supported on porous g-C₃N₄ nanosheets were prepared for efficient reductive amination reactions. The structures of the catalysts were characterized via FTIR, XRD, XPS, SEM, TEM, and TG analysis, and the mechanisms were investigated using in situ ATR–FTIR spectroscopic analysis complemented by theoretical calculation. It transpired that the valence state of the Pd is not the dominating factor; rather, the hydroxyl group of the Pd(OH)₂ cluster is crucial. Thus, by passing protons between different molecules, the hydroxyl group facilitates both the generation of the imine intermediate and the reduction of the C=N unit. As a result, the sterically hindered amines can be obtained at high selectivity (>90%) at room temperature.

Keywords: sterically hindered amine; reductive amination; competing mechanisms; in situ ATR–FTIR analysis; Pd-catalyst



Citation: Hong, Z.; Ge, X.; Zhou, S. Underlying Mechanisms of Reductive Amination on Pd-Catalysts: The Unique Role of Hydroxyl Group in Generating Sterically Hindered Amine. *Int. J. Mol. Sci.* **2022**, *23*, 7621. <https://doi.org/10.3390/ijms23147621>

Academic Editor: Raphaël Schneider

Received: 11 June 2022

Accepted: 8 July 2022

Published: 10 July 2022

Publisher's Note: MDPI stays neutral with regard to jurisdictional claims in published maps and institutional affiliations.



Copyright: © 2022 by the authors. Licensee MDPI, Basel, Switzerland. This article is an open access article distributed under the terms and conditions of the Creative Commons Attribution (CC BY) license (<https://creativecommons.org/licenses/by/4.0/>).

1. Introduction

Amines constitute an indispensable class of chemicals that are widely used as the raw materials or intermediates in the laboratory and in industry to prepare value-added chemicals, such as pharmaceuticals, agrochemicals, and biomolecules [1,2]. To date, numerous organic methodologies for amine production have been reported, such as the aminolysis of haloalkanes [3], the reaction of N-chloro dialkylamines with alkyl Grignard reagents [4], Buchwald–Hartwig and Ullman-type C–N cross-coupling reactions [5,6], as well as reductive amination. The amination of alcohols via so-called borrowing hydrogen (BH) is another important method which is mediated by rare noble-metal catalysts, based on Ru or Ir mostly [7]. Among all these methods, catalytic reductive aminations using molecular hydrogen as the reductant continue to be in the spotlight of both academic and industrial interests, due to their high atom economy and low pollution [8]. As to the catalysts required, in addition to precious metals such as Pd, Pt, Ru, and Rh [9], continuous efforts are being made on employing earth-abundant metals, such as Ni [10], Co [11], and Fe [12] as the active center. By this means, various amines, such as primary, secondary, and tertiary amines with less steric hindrance, can be prepared under moderate conditions [9].

In spite of the numerous studies reported previously on reductive aminations, the associated mechanisms are still disputable and remain ambiguous. It is generally believed that the transformation starts from the formation of imine upon condensation of the carbonyl group with ammonia or amine, followed by the reduction of imine [8]. However, a previous study pointed out that the imine intermediates do not form in the reductive amination with secondary amines [13]. For tertiary amines, the amine forms either by direct hydrogenolysis of the hemiaminal [13,14] or dehydration to enamine followed by

hydrogenation [15]. Most likely, the preference of the reaction pathway depends on both the structure of the reactants and the reaction conditions.

In addition to the ambiguous mechanisms, reductive amination is yet limited for the synthesis of sterically hindered tertiary amines such as non-nucleophilic base and 1,2,2,6,6-Pentamethylpiperidine. In fact, as will be shown later in the Discussion section, we tried a series of commercially available catalysts that are proven to be excellent in mediating the production of most amines via reductive amination; however, most of these catalysts exhibit poor performance in the preparation of *N,N*-diisopropylbutylamine. Notably, Denis Chusov reported an atom-economical method for the synthesis of sterically hindered tertiary amines based on complementary Rh- and Ru-catalyzed direct reductive amination using carbon monoxide as a deoxygenating agent [16]. Indeed, sterically hindered amine is irreplaceable in organic synthesis and catalysis specifically as non-nucleophilic base [17], light stabilizers (HALS) [18], ligands [19], components of frustrated Lewis pairs [20], etc. As far as we know, the sterically hindered amines have been synthesized at industrial scale by reductive amination of carbonyl compounds with poor atom economy reagents such as borohydride reagents. Further efforts are still highly demanding for developing a more efficient preparation of sterically hindered amine via reductive amination with hydrogen.

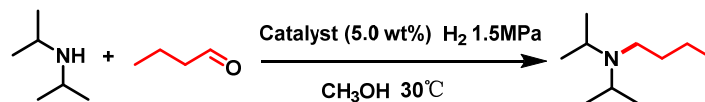
On the other hand, Pd nanoparticles (e.g., Pd/C) have been proven to be efficient for reductive aminations with hydrogen, especially for the synthesis of tertiary amines [21]. Despite the fact that the classic Pd/C-H₂ system is relatively less efficient in mediating the production of sterically hindered amine such as 1-cyclohexylpiperidine [22,23], Pd is still highly promising to complete this task benefiting from relatively strong Pd-C, Pd-H, and Pd-N interactions [24]. To tune the activity of the Pd catalysts, the influences of size effect and the support were investigated. The size distribution of the Pd/C catalyst can be controlled by quite a few strategies by tuning the reducing agents [25] and conditions [26], the concentrations of the stabilizing agent, Pd salt and precipitant [27–29], or introducing a second metal [30]. Support modification is another way to promote the catalytic activity of anchored metal nanoclusters [31]. The graphite-like carbon nitride (g-C₃N₄), characterized as an incompletely condensed, N-bridged “poly(tri-s-triazine)” polymer with lamellar structure, possessed unique physicochemical properties due to its appealing electronic band structure. The nitrogen functionalities on the surface might act as strong Lewis base sites and the π -bonded planar-layered configurations are expected to anchor the substrate and metal active species, making it a privileged candidate for hydrogenation reactions [32–34]. Moreover, treatments with various oxidants to introduce acidic sites on the surface of activated carbon may significantly improve the activity and selectivity of catalysts [35–39]. Up to now, however, it remains to be explored how the support affects selectivity for the production of sterically hindered amines via reductive amination.

In this article, we report an efficient Pd(OH)₂/g-C₃N₄ catalyst for reductive amination. As compared to the previously reported Pd catalysts, the Pd-based nanoparticles prepared in this work are of higher activity and selectivity. By using a combination of structural characterization, in situ spectroscopic investigation, and theoretical calculation, the elaborate structure of the active center, as well as the root cause for the excellent performance of the Pd(OH)₂/g-C₃N₄ catalyst, are revealed.

2. Results and Discussion

2.1. Catalytic Tests of the Prepared Palladium Catalysts

To evaluate the performance of the catalysts studied, the reaction of diisopropylamine with butyraldehyde under hydrogen atmosphere was selected as a model. Various catalysts, including commercially available ones and home-made ones, were employed, and the detailed results are listed in Table 1.

Table 1. Comparisons of the catalytic performance for reductive amination of diisopropylamine with butyraldehyde over various catalysts ^a.

Entry	Catalyst	Temp./°C	Time/h	Conv./%	Sel./%	Yield ^b /%
1	Raney Ni	100	7	70	Trace	Trace
2	Raney Co	30	4	55	Trace	Trace
3	Raney Cu	100	7	46	Trace	Trace
4	5.0 wt% Ru/ACs ^g	30	5	Trace	Trace	Trace
5	5.0 wt% Rh/ACs	30	5	Trace	Trace	Trace
6	5.0 wt% Pt/ACs	30	5	51	61	31
7	5.0 wt% Pd/ACs	30	4	94	85	80
8	1.0 wt% Pd/ACs	30	4	90	76	68
9	Pd(AcO) ₂ +Xphos	60	7	28	46	13
10	10.0 wt% Pd(OH) ₂ /ACs	30	4	97	95	92
11	1.2 ^c , 1.4 ^d , 1.2 ^e wt% Pd(OH) ₂ /ACs	30	4	65/62/33	86 ^c /89 ^d /36 ^e	56/55/12
12	1.1 wt% Pd(OH) ₂ /g-C ₃ N ₄	30	4	60/77	97/95 ^f	58/73(60)
13	1.2 wt% Pd/g-C ₃ N ₄	30	4	33	30	10
14	1.2 wt% Pd/ACs	30	4	80	66	53
15	1.3 wt% PdO/ACs	30	4	22	36	8
16	1.1 wt% PdO/g-C ₃ N ₄	30	4	30	trace	trace

^a Reaction conditions: diisopropylamine (0.1 mol), butyraldehyde (0.05 mol), catalyst loading (0.2 g, 5.0 wt% refer to butyraldehyde), methanol (2.5 mL), and 1.5 H₂ MPa. For Entry 9, Pd(AcO)₂ (0.1 mmol), Xphos (0.1 mmol). ^b Conversion of butyraldehyde and yield of product were determined by gas chromatography. All products (i.e., product amine, n-butanol, and aldol condensation products) were determined by GC-MS. ^c Nitric acid treatment. ^d Hydrothermal treatment. ^e No treatment. ^f 4 Å molecular sieve (0.6 g, 15%), and the value in the brackets represents isolated yield. ^g the “5.0 wt%” represents the metal content in the catalyst, the same as below in Table 1.

To start with, we took commercially 5.0 wt% Pd/ACs as a catalyst to investigate the effect of various conditions for the reaction. We found that the reaction can be proceeded at room temperature, and lower the ratio of amine to aldehyde (<2) or higher hydrogen pressure (>1.5 MPa) improves the selectivity of C=O reduction. Moreover, further prolongation of the reaction time (>4 h) will not bring about the increase in yield. Last but not least, we used methanol as the solvent with additive amount attributing to its high hydrogenation activity for reduction amination [40]. Thus, the optimal conditions for catalyst screening were determined. As shown in Table 1, classic inexpensive hydrogenation catalysts such as Raney Ni/Co/Cu failed to afford the desired product (Table 1, **Entry 1–3**). Next, for the noble-metal catalysts, only Pt/C and Pd/C successfully brought about the generation of diisopropylbutylamine, and Pd/C performed better (Table 1, **Entry 4–8**); however, the competing reduction of C=O was still unavoidable. In addition, atomically dispersed Pd did not give better performance (Table 1, **Entry 9**). Notably, when commercial 10.0 wt% Pd(OH)₂/ACs was employed, the target product was obtained with 92% yield (Table 1, **Entry 10**). This result is consistent with a previous study on Pd(OH)₂/ACs-catalyzed synthesis of tertiary amines [41]. However, when reducing the content of Pd loaded on ACs, the activity of the catalyst decreased dramatically: with ~1.0 wt% Pd, although preliminary nitric acid treatment and hydrothermal treatment of the ACs supports kept the Pd(OH)₂/ACs catalyst at relatively good selectivity, the reaction rate dropped considerably (Table 1, **Entry 10, 11c,d**). To further improve the performance of the Pd catalysts, we changed the support with g-C₃N₄, inspired by the finding of Wang et al. that phenol can be selectively reduced to cyclohexanone at Pd@g-C₃N₄ due to phenol being able to

interact with the surface through the hydroxy group to form strong O–H···N or O–H··· π interactions [34]. We considered that Pd(OH)₂ tends to adsorb on basic sites of g-C₃N₄ by similar O–H···N or O–H··· π interactions. Surprisingly, both the selectivity and the reaction rate maintain simultaneously on 1.1 wt% Pd(OH)₂/g-C₃N₄. By contrast, however, when depositing reduced Pd nanoparticles on g-C₃N₄, the so-obtained Pd/g-C₃N₄ exhibits low catalytic activity (Table 1, Entry 13). Here, the valence state of Pd seems to be important. Thus, further examination on the performance of PdO species was carried out. In contrast to the Pd/support or the Pd(OH)₂/support catalysts, much lower selectivity and yield are given by either PdO/ACs or PdO/g-C₃N₄ (Table 1, Entry 15, 16). Therefore, it is not the high-valence state of Pd that matters; rather, the existence of the hydroxyl group in the Pd-oxide cluster substantially influences the reductive amination processes. Similarly, it has been found previously that the adsorption of hydrogen donors and acceptors on metal catalysts is species-dependent, thus offering opportunities for selectivity control in hydrogen transfer processes [42–44]. Finally, a satisfactory yield was obtained when using 4Å molecular sieve as dehydrating agent (Table 1, Entry 12f). Obviously, here, the reactivity of the system is sufficient, while the conversion is dominated by the reaction equilibrium.

2.2. Characterization of the Prepared Pd(OH)₂/g-C₃N₄ and Other Palladium Catalysts

To reveal the root cause for the excellent performance of Pd(OH)₂/g-C₃N₄, structural characterization is prerequisite. The Fourier-transform infrared (FT-IR) was performed. As shown in Figure 1, the absorption peaks at 1245, 1320, and 1408 cm⁻¹ correspond to the aromatic C–N stretching vibrations, while 1567 and 1640 cm⁻¹ are ascribed to the C=N vibrations. The peak at 808 cm⁻¹ is assigned to the breathing mode of the triazine units (Figure 1c) [45,46]. The broad peak at 3000–3400 cm⁻¹ is ascribed to the stretching vibration of N–H. When loading Pd to the g-C₃N₄, the intensity of these peaks does not change obviously but the intensity of the broad peak at 3000–3400 cm⁻¹ increases (Figure 1a), which can be attributed to the O–H stretching of the Pd(OH)₂. However, intensity of this broad peak decreases with treatment of hydrazine hydrate, indicating that the divalent Pd was reduced partially (Figure 1b). Accordingly, no obvious absorption peak is observed when Pd is loaded on the activated carbons treated by nitric acid or water (Figure 1d–f).

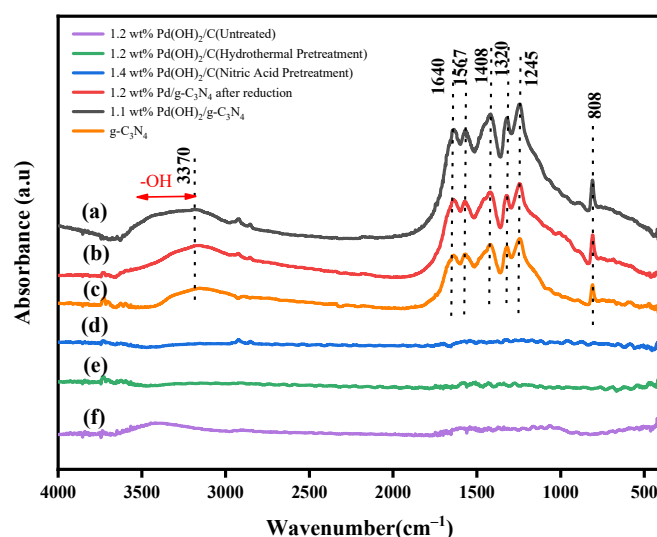


Figure 1. FT-IR spectra of the samples with different of Pd loading determined by ICP-OES.

The phase structure and composition of the selected samples were investigated by X-ray diffraction (XRD). The obtained results are shown in Figure 2. The pattern of g-C₃N₄ is identified by peaks at $2\theta = 27.8^\circ$ and 12.8° , corresponding to the (002) crystallographic plane and (100) planes of in-planar tris-s-triazine structural packing motifs (Figure 2a,b) [47]. The broad peak at 25.1° indicated the typical amorphous structure of activated carbons (Figure 2c–f). The crystal structure of Pd is identified by the diffraction peaks at $2\theta = 40.4^\circ$,

47.0°, and 68.6° (JCPDS 87-0645). These peaks can be assigned to the (111), (200), and (220) planes of Pd metal with a face-centered cubic (fcc) structure, respectively. However, no Pd or PdO characteristic peaks were detected for Pd(OH)₂/g-C₃N₄, suggesting that Pd species may exist in the form of subcrystal or nanoparticles. A weak peak at 40.4° can be observed after reduction (Figure 2b). According to Scherrer's formula [48] and the half-width of the Pd (111) peak, the calculated size of Pd NPs in Pd/g-C₃N₄ is 1.3 nm. When Pd is loaded on ACs, the location of the Pd (111) peak (at 40.4°) remains with a calculated size of Pd 2.4 nm, 3.7 nm, and 2.0 nm. It can be seen that the divalent Pd can be reduced by the reducing groups anchored on the surface of activated carbons during the impregnation process (Figure 2c–e) [49]. Additionally, both PdO/ACs and the commercial 10.0 wt% Pd(OH)₂/ACs catalyst exhibited diffraction peaks at two-theta of 33.5°, 33.8°, 60.2°, and 71.4° in their XRD patterns (Figure S1), which can be indexed as the (101), (112), (103), and (211) diffractions of Palladium oxide (JCPDS 06-0515). Furthermore, the PdH_x phase was not observed in any of the XRD patterns, which is considered as the active species for hydrogenation reactions [50].

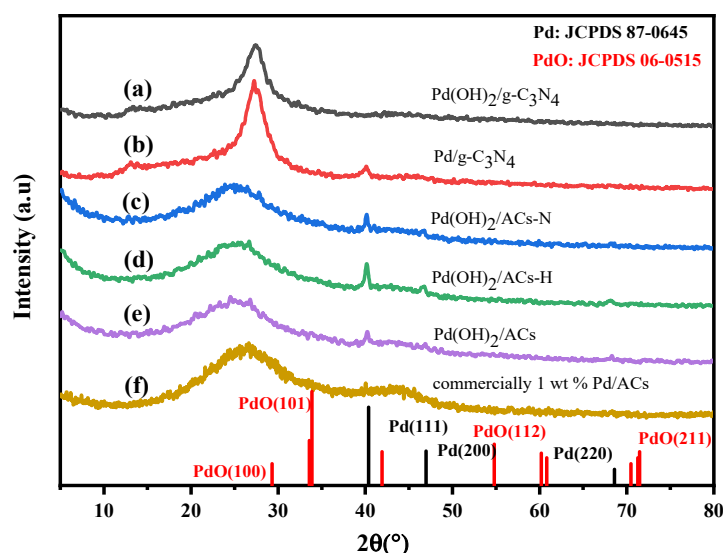


Figure 2. XRD patterns of the selected catalysts. (a) 1.1 wt% Pd(OH)₂/g-C₃N₄, (b) 1.2 wt% Pd/g-C₃N₄, (c) 1.2 wt% Pd(OH)₂/ACs treated by HNO₃ (labelled as Pd(OH)₂/AC-N), (d) 1.4 wt% Pd(OH)₂/ACs after hydrothermal treatment (labelled as Pd(OH)₂/AC-H), (e) 1.2 wt% Pd(OH)₂/ACs without treatment, (f) commercially 1.0 wt% Pd/ACs.

Next, XPS measurements were performed to explore the chemical properties of the surface and the electronic configurations of the active centers. The survey XPS spectrum in Figure 3a shows that C, O, N, and Pd elements coexist in 1.1 wt% Pd(OH)₂/g-C₃N₄ sample. Figure 3b–d show XPS core level spectra of C 1s, N 1s, and Pd 3d of the 1.1 wt% Pd(OH)₂/g-C₃N₄ sample. All lines in the XPS spectra are corrected with carbon C 1s at 284.8 eV. The peak at 284.8 eV in C 1s is attributed to surface adventitious carbon, whereas the peak at 288.2 eV corresponds to sp²-bonded carbon in N–C=N of g-C₃N₄ (Figure 3b). For N 1s, four peaks can be distinguished (Figure 3c). The signal at the binding energy of 398.5 eV is assigned to the pyridinic N (N–C=N), and the peak at 399.9 eV is assigned to the graphitic N. The peaks at 401.0 and 404.6 eV are attributed to the amino group (C–N–H) and some N–O species [33]. The spectra of Pd 3d (Figure 3d) present two doublet peaks, corresponding to the spin–orbital splitting of Pd 3d_{5/2} and Pd 3d_{3/2} for two types of Pd species. The peaks at 335–336 eV can be assigned to reduced Pd and the ones at 336–337 eV to palladium oxide or palladium hydroxides. It has been pointed out previously that Pd(OH)₂ on carbon materials is a core–shell structure of C/PdO/OH/H₂O [51]. The ratio of Pd⁰ to Pd²⁺ was about 31:69 using Gaussian/Lorentzian line shape approximations, suggesting that the Pd atoms in Pd(OH)₂ are partially reduced during the preparation

(see Figures S3 and S4). After treatment with hydrazine hydrate, the ratio of Pd⁰ to Pd²⁺ increases to 70:30 (Figure S2). Thus, the bivalent palladium species was considered as the main active component in the reaction. To our surprise, the content of pyridinic N decreased from 76% to 74% and the content of graphitic N increased from 16% to 19% when the catalyst was treated by hydrazine hydrate (see Figure 2c and Figure S2c). Previous reports revealed that pyridinic coordination sites exhibited the highest metal-loading stability, whereas the graphitic-N coordination sites had the least stable one [33,52]. We infer that the Pd species may aggregate during reduction by hydrazine hydrate. On the other hand, N 1s signals of Pd/g-C₃N₄ shift 0.05 eV towards low binding energy, indicating that the interaction between the g-C₃N₄ and Pd is weakened after reduction. For Pd(OH)₂/ACs, the one whose support is hydrothermally treated possesses more phenolic groups on the surface (Figures S3c and S4c). Notably, the Pd 3d_{5/2} peak for the Pd species on the hydrothermally treated supports is 0.8 eV higher than that of the nitric acid treatment supports, as depicted in Figures S3d and S4d, indicating the presence of a strong interaction between the support and Pd. According to the literature, Pd species can be stabilized by the deprotonation process between the Pd precursor and phenolic groups (–OH) to produce an oxygen anion (–O–) and facilitate the dispersion of Pd [39,53].

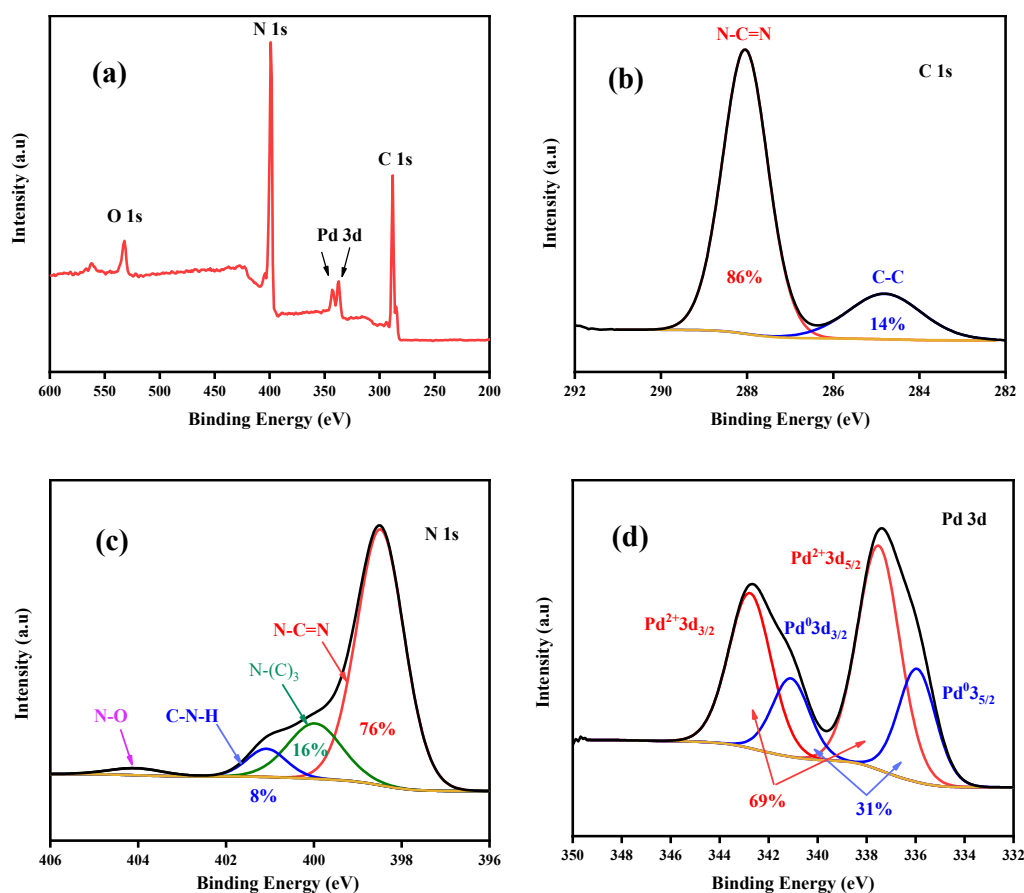


Figure 3. XPS spectra of 1.1 wt% Pd(OH)₂/g-C₃N₄: (a) the survey spectrum; (b) the core-level spectrum of C1s; (c) the core-level spectrum of N 1s; (d) the core-level spectrum of Pd 3d_{5/2} and 3d_{3/2} doublet region.

In order to identify the morphology of the Pd species on g-C₃N₄, scanning electron microscopy (SEM) and transmission electron microscopy (TEM) were performed for Pd(OH)₂/g-C₃N₄. The SEM image (Figure 4a) demonstrates that the Pd(OH)₂/g-C₃N₄ composite possesses a fluffy, wrinkled, and porous microstructure. Meanwhile, it can be seen from the TEM images (Figure 4c) that the Pd species were distributed throughout the g-C₃N₄ architecture uniformly without obvious aggregation, disclosing that the nanosheets

are layered flakes and possess some defects and voids which provide abundant anchoring sites for Pd species. The average particle size of the Pd nanoparticles in Pd(OH)₂/g-C₃N₄ is 2.11 nm, as determined by statistical evaluation of 100 particles in the TEM images. The Pd content of the Pd(OH)₂/g-C₃N₄ and Pd/g-C₃N₄ sample determined by ICP-OES is calculated to be 1.1 wt% and 1.2 wt%.

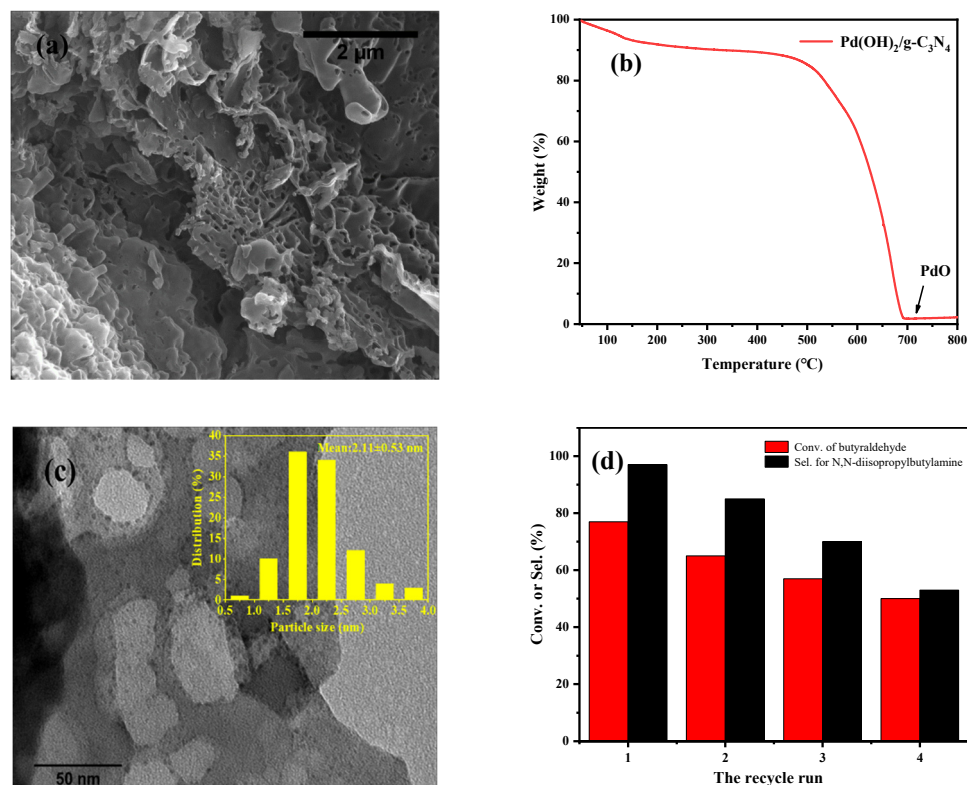


Figure 4. SEM (a) and TEM (c) images of Pd(OH)₂/g-C₃N₄, (b) Thermogravimetric plots for Pd(OH)₂/g-C₃N₄ and the size distribution of Pd species on Pd(OH)₂/g-C₃N₄. (d) Reuse of 1.1 wt% Pd(OH)₂/g-C₃N₄ catalyst at same conditions.

Subsequently, according to the thermogravimetric (TG) analysis, for Pd(OH)₂/g-C₃N₄, there is an initial weight loss ~135 °C which is due to the removal of adsorbed water molecules within the system. After that, the Pd(OH)₂/g-C₃N₄ sample is stable up to 500 °C and starts to decompose and decomposition is complete ~680 °C with a residual weight of 2.0% (Figure 4b); this decomposing temperature is higher compared to Pd/g-C₃N₄ [54]. Alternatively, the thermal stability of the catalyst can also be improved by introducing hydroxyl groups to the support-activated carbons with hydrothermal treatment (Figure S5). Thus, the presence of the hydroxyl groups enhances the thermal stability of the catalyst. Furthermore, for the heterogeneous catalysis reaction, it is important to test the reusability of the catalyst. Thus, the reusability of the 1.1 wt% Pd(OH)₂/g-C₃N₄ catalyst was investigated using the reductive amination of diisopropylamine with butyraldehyde as a model reaction. Moderate selectivity toward N,N-diisopropylbutylamine was obtained after four runs (Figure 4d), suggesting that this catalyst has acceptable reusability.

2.3. Mechanism Studies

Upon addressing the structural features of different catalysts and recycling tests, the in situ ATR-FTIR spectroscopic analysis was employed to identify how the catalysts interact with the substrates during the reductive amination. The peaks of $\nu(\text{C}=\text{O})=1740\text{--}1780\text{ cm}^{-1}$ were firstly identified for all the spectra [55]. For commercial 1.0 wt% Pd/ACs, the imine species $\nu(\text{C}=\text{N})=1625\text{ cm}^{-1}$ with weak intensity was observed when acetaldehyde and ammonia were introduced to the in situ reaction cell [56]. This peak decreased but did

not disappear when continuously introducing H_2 (Figure 5a) into the system. Meanwhile, the $[\nu(C-N)]$ mode in the range of $1350\text{--}1280\text{ cm}^{-1}$ cannot be observed, probably due to its low intensity [57,58]. Note that there is no stretching vibration peak of water at $3200\text{--}3500\text{ cm}^{-1}$, indicating that the dehydration process may not require a catalyst [59]. It is also confirmed by the fact that ethanimine formed without a catalyst (See Figure S6). The $C=N$ vibration was also observed when acetone and NH_3 were introduced into the cell, and a peak around 3464 cm^{-1} was observed (Figure 5b). Considering the $[\nu(O-H)]$ stretching mode adjacent to the nitrogen atom; most likely, this hydroxyl group belongs to the hemiaminal intermediate [60]. The peaks at 1200 cm^{-1} and 1130 cm^{-1} were assigned to the deformation stretching of the $C-N$ bond (Figure 5c) [57]. The imine mechanism thus prevails as well. By contrast, for the secondary amine diethylamine, a broad peak located at $3200\text{--}3600\text{ cm}^{-1}$ emerged only after H_2 was introduced. This can be ascribed to the stretching vibration of adsorbed water, which was further proven by the peak in 1640 cm^{-1} (assigned to the $H-O-H$ bending bands in product water) (Figure 5d) [59]. Meanwhile, the skeleton-stretching vibration of $(-C_3)N$ [$\nu((-C_3)N)=1178\text{ cm}^{-1}$] is also identified [58], suggesting that the dehydration and hydrogenation processes occur simultaneously on the surface of the catalyst. As for the amination of diisopropylamine, the commercial 1.0 wt% Pd/ACs, $Pd(OH)_2/g-C_3N_4$, $Pd/g-C_3N_4$, and $PdO/g-C_3N_4$ were compared (Figure 5e–h). For all catalysts, a weak peak, as discussed above, assigned to the stretching vibration of the hydroxyl group of the hemiaminal, appeared at 3487 cm^{-1} , 3491 cm^{-1} , 3474 cm^{-1} , and 3483 cm^{-1} , respectively, after introducing diisopropylamine and acetaldehyde to the in situ reaction cell. They were found as red-shift peaks due to the difference of surface binding or adsorption strength between the different Pd catalysts since the hydroxyl group vibration of the free hemiaminal is 3628 cm^{-1} , according to DFT calculation at the B3LYP/6-31+(g) level. The peak of the water shows a completely different shape difference, which may imply a completely different catalytic performance on the home-made catalysts. Except for $PdO/g-C_3N_4$, all the other catalysts show the peaks of adsorbed water, which is in line with the experimental results that home-made $PdO/g-C_3N_4$ is inactive. Moreover, no imine peak at the range $1620\text{--}1680\text{ cm}^{-1}$ was observed [56]. The identification of the product might be difficult because of the low intensity of the typical band at $1220\text{--}1270\text{ cm}^{-1}$ assigned for the skeleton-stretching vibration of $(-C_3)N$ [58].

Based on the in situ characterization, the reaction mechanisms were investigated by theoretical calculations. Considering the different performances of $Pd/g-C_3N_4$ and $Pd(OH)_2/g-C_3N_4$, the valence state of Pd matters for the reductive amination of diisopropylamine. The generation of imines for different substrates was examined computationally, concerning both the hydrogen transfer and dehydration processes (see Figures S7–S10). They are all kinetically less favorable due to high reaction barriers ($>40\text{ kcal/mol}$). However, when a second amine is introduced into the reaction complex, the subsequent reaction barrier for both hydrogen transfer and dehydration is lowered by 2 kcal/mol and 10 kcal/mol , respectively. Further enhancement in these two steps is achieved when a third amine is introduced (see Figure S11). It seems that dehydration from aldehydes and primary amines or ammonia is a multimolecule synergistic process. This result is in line with the in situ ATR-FTIR spectroscopic findings (see Figure S6). On the contrary, for imine hydrogenation, a catalyst is required since the reaction barrier is extremely high ($>60\text{ kcal/mol}$; see Figure S12).

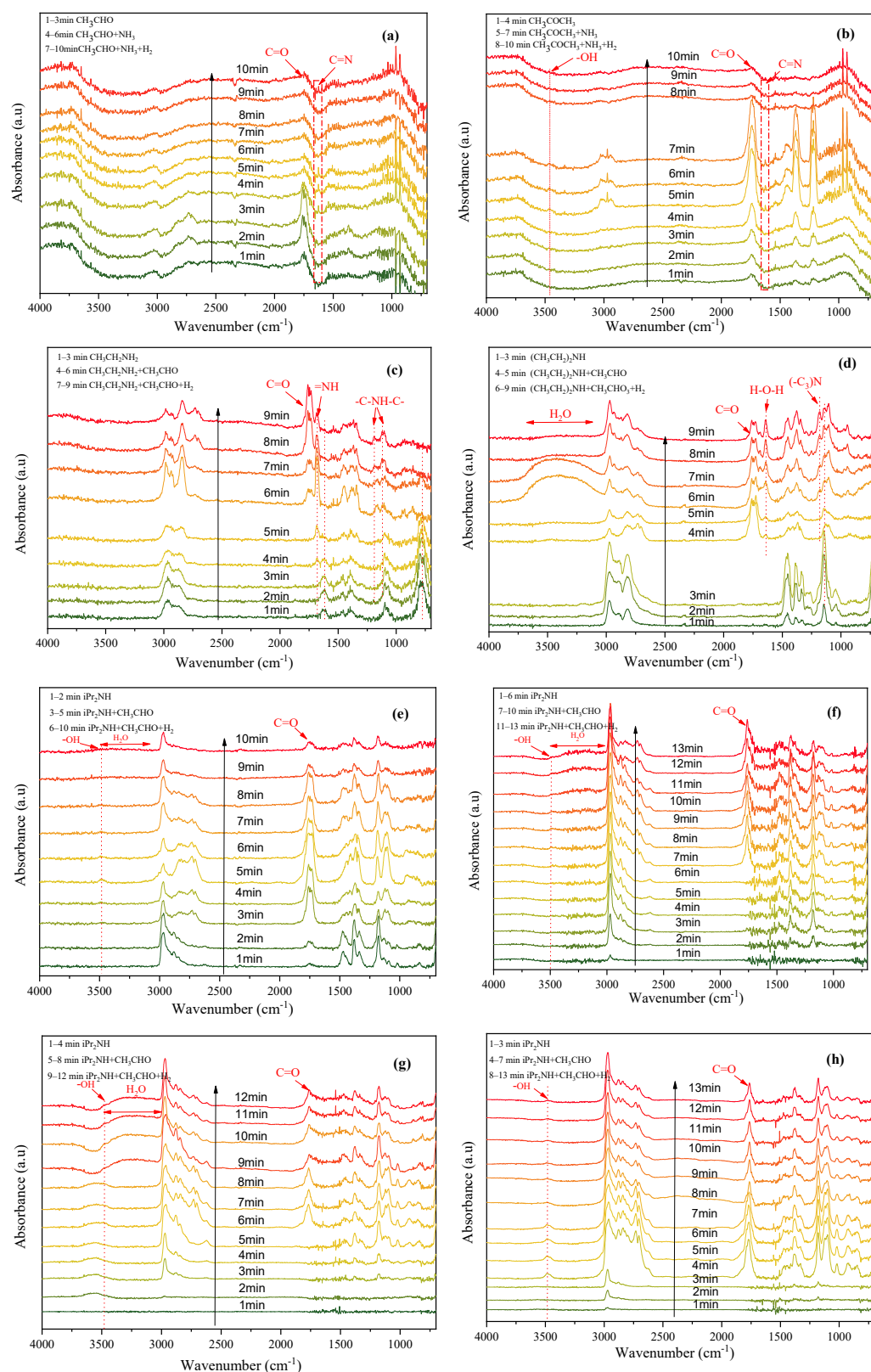


Figure 5. ATR-FTIR spectra recorded during hydrogenation of different substrates: (a) CH₃CHO and NH₃, (b) CH₃COCH₃ and NH₃, (c) CH₃CH₂NH₂ and CH₃CHO, (d) (CH₃CH₂)₂NH and CH₃CHO, (e) iPr₂NH and CH₃CHO, (f) iPr₂NH and CH₃CHO. (a–e) commercial 1.0 wt% Pd/ACs, (f) 1.1 wt% Pd(OH)₂/g-C₃N₄, (g) 1.2 wt% Pd/g-C₃N₄, (h) 1.1 wt% PdO/g-C₃N₄. The “1.0 wt%” represents the Pd content in the catalyst, and in the other cases the Pd loading was determined by ICP-OES.

Thus, the Pd(111) plane was used for modeling the Pd/g-C₃N₄ catalyst to understand the catalytic performance on Pd⁰ species. We first investigated the adsorption behavior of hydrogen on the Pd(111) surface, demonstrating that the hydrogen is preferentially absorbed on the bridge and hollow sites (see Figure S13). Furthermore, as shown in Figure 6, initially diisopropylamine and acetaldehyde are coadsorbed on the Pd(111) surface. The N–H bond activation of diisopropylamine takes place upon hydrogen transfer from the nitrogen atom to the oxygen atom via **TS1/2**, and C–N coupling takes place spontaneously (**IM1** → **IM2**). Species adsorption on the catalyst surface significantly lowers the reaction energy barrier, making it feasible under mild conditions (see Figure S10). Next, palladium hydride attacks the oxygen atom, thus breaking the C–O bond via **TS3/4**, which was identified as the rate-determining step (RDS). After that, **IM4** is generated, which further releases a water molecule to form **IM5**. Finally, by transferring a hydrogen atom from the Pd surface to N, an intact N,N-Diisopropylethylamine molecule is produced (**IM6**). This process is featured as the hydrogenolysis mechanism [61]. In addition to the pathways via hydrogenolysis, an alternative imine path was also investigated [62]. Specifically, after the imine intermediate is generated via **TS7/8**, hydrogen transfer from Pd to C affords the target product (**IM9** → **IM10**). This step is followed by further hydrogenation of the hydroxyl groups, thus generating a water molecule (**IM12**). Comparing the above two pathways, the latter is energetically more favorable. Furthermore, we examined theoretically the hydrogenation of the acetaldehyde on the Pd(111) surface. As shown in Figure S14, the H atoms are successively added to O and C in a step-wise manner via the sequence **IM13** → **TS13/14** → **IM14** → **IM15** → **TS15/16** → **IM16**. Alternatively, the H atoms are successively added to C and O in a step-wise manner via the sequence **IM17** → **TS17/18** → **IM18** → **IM19** → **TS19/20** → **IM20**. Although the former is thermodynamically more favorable due to its high exothermicity (−81 kcal/mol), the latter is kinetically more preferred due to the low barrier for the hydrogenation process.

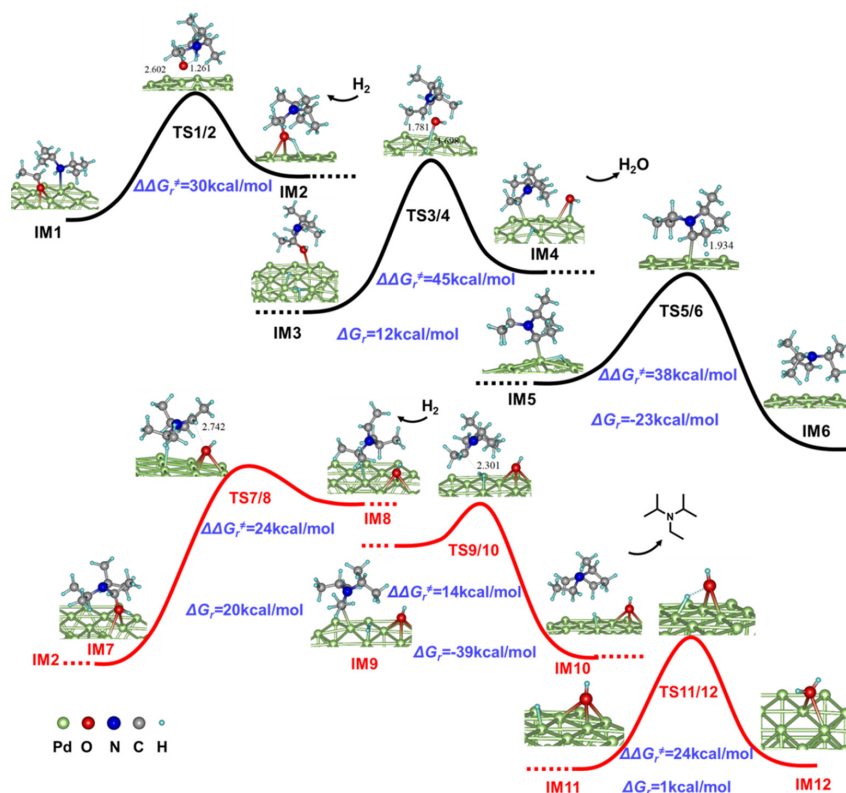


Figure 6. Simplified PES and selected structural information of alternative pathways for the generation of N,N-Diisopropylethylamine mediated by the Pd(111) plane via hydrogenolysis (black) and imine (red) mechanisms.

For Pd(OH)₂/g-C₃N₄, considering the structure characterized previously [51], a Pd₈O₁₂H₈ cluster was used to simulate the reductive amination processes. As shown in Figure 7, when diisopropylamine and acetaldehyde are coadsorbed on the clusters, the hemiaminal intermediate is formed spontaneously without a reaction barrier by simple hydrogen exchange between diisopropylamine and a hydroxyl group (IM21 → IM22). On the contrary, the reaction barrier for forming a hemiaminal on the PdO cluster is extremely high (45 kcal/mol; see Figure S15), making PdO/g-C₃N₄ inactive. Here, the presence of the O–Pd–OH site is crucial. We first consider that the hydrogenolysis process occurs on the clusters which is similar to that on the Pd(111) surface. The transitional structure involving palladium hydride attacking the oxygen atom to form a water molecule was firstly located. However, the subsequent hydrogenation transition state structure could not be found (see Figure S16). After breaking the C–O bond (IM23 → → IM24), the hydroxyl group on the catalyst surface serves as a “courier” to pass hydrogen. Thus, a water molecule forms first by hydrogen transfer from Pd to OH via TS25/26. Next, a hydrogen atom on the so-formed water molecule migrates to the imine carbon to form the product (IM26 → → IM27). Here, we considered that the imine species can be polarized by a hydrogen bond formed between N and a hydrogen atom on the so-formed water, thus increasing the probability to generate a transition state for H addition. Finally, by transferring a second hydrogen atom from Pd OH, an intact water molecule forms again (IM28). This process is similar to phenol acting as a conduit to transfer a proton from the hydronium ion (with an accompanying charge transfer from the metal surface) to the basic carbonyl oxygen of the benzaldehyde via a PCET mechanism in the electrochemical hydrogenation (ECH) system, as reported by Udishnu Sanyal et al. [63]. Moreover, a thermodynamically more favorable pathway (−49 kcal/mol) was also found via the sequence IM25 → TS25/26 → IM26 → IM29 → TS29/30 → IM30. Considering the difference in the reaction pathways presented in Pd(111) and the Pd cluster, the hydroxyl group is unique in that: (1) via barrierless (or quasi-) proton exchange, the formation of a hemiaminal is facilitated at the O–Pd–OH site; (2) the hydroxyl group serves as a hydrogen shuttle in the reduction of the imine unit concerted with the dihydrogen activation; (3) the Pd nanoclusters may be stably anchored on the basic sites of g-C₃N₄ by forming strong O–H···N or O–H···π interactions. In spite of the lower energy barrier for the hydrogenation of acetaldehyde (see Figure S17), the surface of the cluster preferentially adsorbs the hemiaminal intermediate by similarly forming O–H···N interactions which are generated spontaneously in advance. A high selectivity for reductive amination thus results, in line with the experimental findings. The probable mechanism for the generation of diisopropylethylamine is shown in Scheme 1, and the Figure S18 showed the intact outline for the generation of diisopropylethylamine catalyzed by a Pd₈O₁₂H₈ cluster.

To examine the versatility of the reduction amination on Pd(OH)₂/g-C₃N₄, various aldehydes and amines (mainly secondary ones) were used as the substrates (Table 2), especially for the ones with sterically hindered groups. For paraformaldehyde as a substrate, higher temperature (363 K) and more methanol (10 mL) were acquired to dissolve it. Other reaction conditions are similar with reported in Table 1. As for diisopropylamine and aliphatic aldehyde (Entry 1,2), the selectivity to the corresponding tertiary amine could reach 99 and 87%, respectively. Piperidines (Entry 3–6) gave a similar result to diisopropylamine (Entry 1). However, the selectivity of the target tertiary amine dropped as expected when acetaldehyde was employed due to its higher reactivity that can launch the reduction of the carbonyl group and aldol condensation (Entry 7,8) [22]. Apart from piperidines, the chain secondary amine (Entry 9) could also afford relatively high conversion and selectivity. Unfortunately, when aromatic amines such as diphenylamine and N-ethylaniline were employed (Entry 10,11), the selectivity and yield were significantly decreased due to the competing C–N activation processes [64]. On the contrary, dicyclohexylamine (Entry 12) could be transformed with 99% conversion and 99% selectivity. As for cyclohexylamine (Entry 13), the conversion and selectivity could reach 70% and 75%, respectively. The

^1H and ^{13}C NMR spectra of all products can be found in the Supplementary Materials (Figure S19–S46).

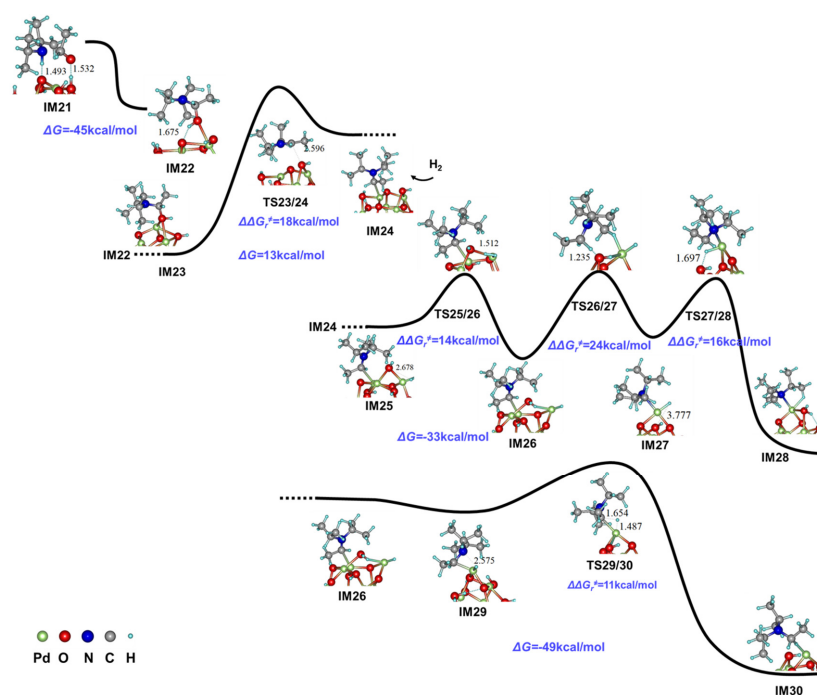
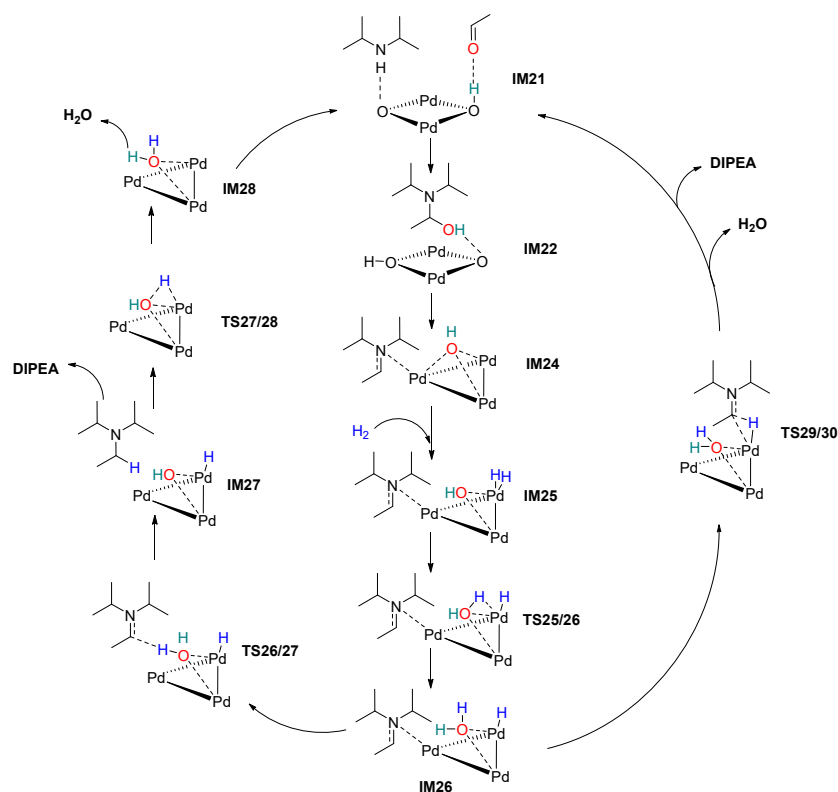
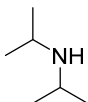
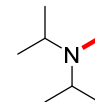
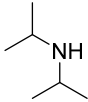
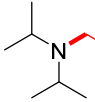
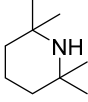
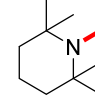
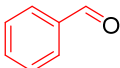
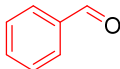
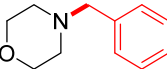
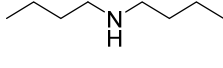
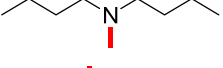
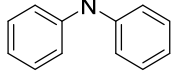
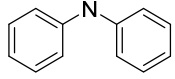
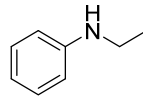
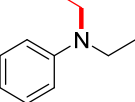
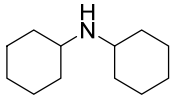
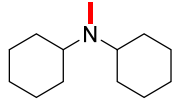
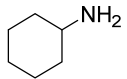


Figure 7. Simplified PES and selected structural information of alternative pathways for the generation of *N,N*-Diisopropylethylamine mediated by the $\text{Pd}_8\text{O}_{12}\text{H}_8$ cluster.



Scheme 1. Proposed mechanism for the generation of *N,N*-Diisopropylethylamine mediated by the $\text{Pd}_8\text{O}_{12}\text{H}_8$ cluster.

Table 2. Reductive Amination Towards Aldehydes and Amines catalyzed by Pd(OH)₂/g-C₃N₄.

$\text{R}_1\text{NHR}_2 + \text{R}_3\text{CHO} \xrightarrow[\text{CH}_3\text{OH}]{\text{Pd(OH)}_2/\text{g-C}_3\text{N}_4, \text{H}_2} \text{R}_1\text{N(R}_2\text{)R}_3$			Temp (°C)	t (h)	Conv. (%)	Sel. (%)	Yield. ^a (%)	
Entry	Sub 1	Sub 2	Product					
1		(CHO) _n		90	6	90	>99	>89(83)
2				30	6	99	87	86(81)
3		(CHO) _n		90	6	>99	>99	>99(98)
4				90	6	>99	>99	>99(93)
5		(CHO) _n		90	6	>99	>99	>99(94)
6				90	6	85	85	72(62)
7				30	6	>99	70	70(63)
8				30	6	90	40	36(28)
9		(CHO) _n		90	6	>99	>99	>99(98)
10		(CHO) _n		90	6	85	12	10(8)
11				30	6	40	38	15(12)
12		(CHO) _n		90	6	>99	>99	>99(92)
13		(CHO) _n		90	6	70	75	52(43)

Reaction conditions: catalyst loading (5.0 wt%, refer to sub 2, 1.1 wt% Pd(OH)₂/g-C₃N₄), sub 1 (0.1 mol), sub 2 (0.05 mol). For cases using paraformaldehyde (degree of polymerization (DP) = 3) as substrate, the usage of methanol is 10 mL, other cases are 2.5 mL. The actual molar ratio formaldehyde: amine is 1.5:1. All products were determined by GC-MS.^a Isolated yields are reported in the brackets. All the products were separated and purified by vacuum distillation or silica gel column chromatography (see Section 3.4 for more details).

3. Materials and Methods

3.1. Chemicals and Materials

Palladium dichloride (PdCl_2), palladium oxide (PdO), and 10.0 wt% $\text{Pd(OH)}_2/\text{ACs}$ were purchased from Alfa Aesar. Diisopropylamine, butyraldehyde, activated carbon, melamine, cyanuric acid, methanol, and molecular sieve were obtained from Sinopharm Chemical Reagent Co., Ltd. Water was purified by ion exchange and used as deionized water. Other chemicals were of analytical purity and were used as received.

3.2. Characterization Techniques

The X-ray diffraction (XRD) patterns of the samples were recorded using a Shimadzu X-ray diffractometer (MAXima XRD-7000, the Japan) with $\text{Cu K}\alpha$ radiation at 40 kV and 40 mA. The X-ray photoelectron spectroscopy (XPS) measurements were performed on a Thermo Scientific K-Alpha+ system using $\text{Al K}\alpha$ radiation (1486.6 eV) under a base pressure of 2×10^{-7} Torr. A FEI QUANTA FEG 650 field emission scanning electron microscope (SEM) operated at 30 kV and transmission electron microscopy (TEM) using a HT-7700 (Tokyo, Japan) at 100 kV were used for determining the morphology of the as-synthesized Pd catalysts. The Pd loading in the materials was analyzed by an Agilent 720ES type inductively coupled plasma optical emission spectroscopy (ICP-OES) instrument. The FTIR spectra were recorded using a Thermo Scientific Nicolet iS50 FTIR spectrometer, and in situ FT-IR (ATR-FT-IR) spectra were recorded using the same spectrometer with ATR appendix. The thermal gravimetric analysis (TGA) was performed by using the Pyris 1 TGA thermogravimetric analyzer with a heating rate of $5^\circ\text{C}/\text{min}$ under nitrogen atmosphere. All products were determined by 7820A-5977B GC-MS (Agilent Technologies, CA, USA) using HP-5MS column. ^1H NMR and ^{13}C NMR were recorded on a Bruker AVANCE III 400 MHz (101 MHz for ^{13}C), using deuterated chloroform (CDCl_3) and tetramethylsilane (TMS, $\delta = 0$) as internal reference. Chemical shifts are reported in parts per million (ppm) downfield and quoted to the nearest 0.01 ppm relative to the residual protons in the NMR solvent (^1H NMR: δ 7.26 ppm, ^{13}C NMR: δ 77.16 ppm), and coupling constants (J) are quoted in Hertz. GC analyses were performed on an Agilent 5973–6890 series gas chromatograph system (Agilent Technologies, CA, USA) equipped with a flame ionization detector (FID). All the separations were performed on a weakly polar capillary column SE-30.

3.3. Preparation of the Supports and Palladium Catalysts

3.3.1. Preparation of g- C_3N_4 Support

Bulk g- C_3N_4 was synthesized by a thermal treatment of a mixture of melamine and cyanuric acid with a weight ratio of 1:1 [65]. All chemicals used in the preparation were of analytical grade without further treatment. Typically, 10 g above precursor powder was placed in an alumina crucible without a cover. Then, the crucible was placed in the middle section of a tube. After vacuuming the tube, argon gas was continuously fed in with a flow rate of 50 mL min^{-1} during the thermal treatment. The sample was heated to 120°C at a rate of $10^\circ\text{C}\cdot\text{min}^{-1}$, and maintained at this temperature for 20 min. The mixture was then heated to 550°C and calcinated for 5 h. After cooling to room temperature, ~ 1700 mg of bulk g- C_3N_4 was obtained.

3.3.2. Pretreatment of Activated Carbon

The pretreatment of ACs has been reported elsewhere previously [38,39]. The activated carbon was pretreated with 0.4N of HNO_3 at 353 K for 4 h, was then washed with distilled water until $\text{pH} = 7$ after cooling to room temperature, and eventually dried in a vacuum at 323 K overnight. For hydrothermal treatment, 40 mL of deionized water was introduced into a 100 mL high-pressure autoclave; then, it was heated to 453 K and the pressure was self-generated, held at that temperature for 2 h, and subsequently cooled to room temperature. The treated ACs were filtered from the slurry and dried at 323 K overnight.

3.3.3. Preparation of the Pd/ACs Catalyst

Pd/ACs catalysts were synthesized by wetness impregnation method. First, 30 mg PdCl₂ was dissolved into 10 mL water with HCl mixture solution (volume/volume = 10:1). Then, the treated ACs (the ratio of ACs to water was 1 g/10 mL) were introduced into the PdCl₂ solution and the slurry was vigorously stirred at 353 K for 4 h; then, the slurry solution pH of 8–9 was reached by dropwise addition of KOH aqueous solution (10%). Eventually, the precipitated Pd(OH)₂ supported on ACs was reduced by 50% hydrazine hydrate at room temperature, filtered, and dried in vacuum at 323 K overnight.

3.3.4. Preparation of the Pd(OH)₂/g-C₃N₄ and Pd(OH)₂/ACs Catalysts

The Pd(OH)₂/C₃N₄ and Pd(OH)₂/ACs catalysts were synthesized with similar method without further reduction. First, 30 mg PdCl₂ was dissolved into 10 mL water with HCl mixture solution (volume/volume = 10:1). The PdCl₂ solution pH of 8–9 was reached by dropwise addition of KOH aqueous solution (10%). Then, the slurry was mixed with 1 g g-C₃N₄ and vigorously stirred at 323 K in a three-neck flask for 4 h, then filtered and dried in vacuum at 323 K overnight. This was the same procedure as Pd(OH)₂/ACs catalyst. PdO/ACs was prepared using PdO as precursor instead of the Pd(OH)₂ deposition.

3.4. General Procedure for the Preparation of Sterically Hindered Amine and Recycling Experiments

Diisopropylamine (0.1 mol) and butyraldehyde (0.05 mol), 5.0 wt% catalyst (0.2 g), and methanol (2.5 mL) were mixed into 100 mL high-pressure autoclave at 30 °C. Then, 1.5 MPa H₂ was fed into the reaction mixture. The mixture was stirred at 1000 rpm at 30 °C for 4 h. After the reaction, the rest of H₂ was discharged. The conversion of the butyraldehyde and the sterically hindered amine yields were determined by GC with triethylamine as the internal standard. After the reaction, the catalyst was filtered and exhaustively washed with methanol, and dried in vacuum at 323 K for 12 h. The collected catalyst was used for the next run under the same conditions. Other cycles were repeated following a similar procedure. All the products were separated and purified by vacuum distillation or silica gel column chromatography. For **Entry 12** in Table 1 and **Entry 1–3, 5, 9, 12** in Table 2, the products were separated via vacuum distillation in a rotary evaporator; for **Entry 7, 8, 13** in Table 2, the products were separated via vacuum distillation in a rotary evaporator to remove the solvent and then vacuum rectification with a home-made rectification column using spring packing; for **Entry 4, 6, 10, and 11** in Table 2, the products were purified by silica gel column chromatography.

The efficiency of the catalyst was characterized by calculating the conversion (*Conv.*%) of butyraldehyde (*BA*) based on the following equation (Equation (1)):

$$\text{Conv.\%} = \frac{n_{\text{consumed BA}}}{n_{\text{initial BA}}} \cdot 100 \quad (1)$$

Sterically hindered amine (*AN*) yield (*Y*%) was also calculated as follows (Equation (2)):

$$\text{Yield\%} = \frac{n_{\text{formed AN}}}{n_{\text{theoretical AN}}} \cdot 100 \quad (2)$$

Furthermore, *AN* selectivity (*Sel.*%) was calculated according to the following equation (Equation (3)):

$$\text{Sel.\%} = \frac{n_{\text{formed AN}}}{\sum n_{\text{products}}} \cdot 100 \quad (3)$$

3.5. General Operation Procedure for the In Situ FT-IR Spectra

In situ FT-IR spectra to investigate the adsorption of different acetaldehyde and diisopropylamine on Pd catalyst were recorded on a Nicolet iS50 spectrometer equipped with a cell fitted with BaF₂ windows and an MCT-A detector cooled with liquid nitrogen.

The spectrum was collected at a resolution of 4 cm^{-1} with an accumulation of 32 scans in the range of $4000\text{--}700\text{ cm}^{-1}$. Here, the interaction of acetaldehyde and diisopropylamine was taken as an example (Figure 5f), and the catalyst sample (25 mg) was filled in priorly into a self-supported wafer. Then, the sample wafer was pretreated under a flow of N_2 for 30 min at room temperature to remove the impurities absorbed on the surface. The background was collected at room temperature under a flow of N_2 . Then, liquid diisopropylamine (2 mL) filled into a glass tube was firstly vaporized by heating belt flowing by N_2 to sample wafer. Considering that pursuing a spectrum with acceptable adsorption intensity and liquefaction of substrates on the surface of the catalyst should be avoided, the temperature of the sample wafer was chosen as 323 K for all the catalysts. The spectra of adsorption of diisopropylamine were recorded per minute until stable spectra were obtained. Then, acetaldehyde (2 mL) was vaporized by heating belt to sample wafer as well. The spectra of coadsorption of diisopropylamine and acetaldehyde were recorded per minute until stable spectra were obtained. Finally, the system was purged with a flow of hydrogen instead of N_2 to obtain the spectra of aldehyde/amine/ H_2 mixture. After a stable spectrum was obtained, the system was purged with a flow of N_2 again, and the desorption spectra were recorded toward the desorption time until there was no change in the band intensity. Other catalysts were then tested in a similar manner.

3.6. Computational Details

The structural optimization and the frequency analysis were performed at the GFN-xTB level of the xTB package [66,67]. Stationary points were optimized without symmetry constraint, and their nature was confirmed by vibrational frequency analysis. Unscaled vibrational frequencies were used to correct the relative energies for zero-point vibrational energy (ZPVE) contributions. Intrinsic reaction coordinate (IRC) [68–70] calculations were also performed to link transition structures with the respective intermediates; to achieve this, a Gaussian interface to the xTB code “gau_xtb” was employed [71].

4. Conclusions

In summary, a highly selective Pd catalyst designed specifically for the preparation of sterically hindered amine was reported. The selectivity of diisopropylbutylamine was up to 97%, and the yield of product amounted to 73%. The catalyst was characterized using FTIR, XRD, XPS, SEM, TEM, and TG, indicating that the active metal was well dispersed on $\text{g-C}_3\text{N}_4$ and stabilized by the hydroxyl group. The in situ ATR-FTIR measurement, together with the theoretical calculations, reveal that the generation of a key intermediate hemiaminal was facilitated by the proton exchange process, and the preferential adsorption of the hemiaminal enabled the selective reduction amination of diisopropylamine to sterically hindered amine. Here, the bifunctionality of the hydroxyl group mattered. An imine mechanism was thus justified for the generation of sterically hindered tertiary amines. Our work shed light on the catalytic mechanisms of reductive amination; in particular, the critical role of the hydroxyl group in the generation of sterically hindered tertiary amine was revealed. Hopefully, this may be instructive for the construction of amine moieties in specific molecules.

Supplementary Materials: The following supporting information can be downloaded at: <https://www.mdpi.com/article/10.3390/ijms23147621/s1>.

Author Contributions: Conceptualization and supervision, X.G. and S.Z.; methodology, software, writing—original draft preparation, Z.H. All authors have read and agreed to the published version of the manuscript.

Funding: Generous financial support by the National Natural Science Foundation of China (21878265, 22078130).

Institutional Review Board Statement: Not applicable.

Informed Consent Statement: Not applicable.

Data Availability Statement: Additional figures are available in the Supplementary Materials.

Conflicts of Interest: The authors declare no conflict of interest.

References

1. Afanasyev, O.I.; Kuchuk, E.; Usanov, D.L.; Chusov, D. Reductive Amination in the Synthesis of Pharmaceuticals. *Chem. Rev.* **2019**, *119*, 11857–11911. [[CrossRef](#)] [[PubMed](#)]
2. Smith, A.M.; Whyman, R. Review of Methods for the Catalytic Hydrogenation of Carboxamides. *Chem. Rev.* **2014**, *114*, 5477–5510. [[CrossRef](#)] [[PubMed](#)]
3. Shamim, T.; Kumar, V.; Paul, S. Silica-Functionalized CuI: An Efficient and Selective Catalyst for N-Benzoylation, Allylation, and Alkylation of Primary and Secondary Amines in Water. *Synth. Commun.* **2014**, *44*, 620–632. [[CrossRef](#)]
4. Coleman, G.H. The Reaction of Alkylchloroamines with Grignard Reagents. *J. Am. Chem. Soc.* **1933**, *55*, 3001–3005. [[CrossRef](#)]
5. Ruiz-Castillo, P.; Buchwald, S.L. Applications of Palladium-Catalyzed C–N Cross-Coupling Reactions. *Chem. Rev.* **2016**, *116*, 12564–12649. [[CrossRef](#)]
6. Sambigao, C.; Marsden, S.P.; Blacker, A.J.; McGowan, P.C. Copper catalysed Ullmann type chemistry: From mechanistic aspects to modern development. *Chem. Soc. Rev.* **2014**, *43*, 3525–3550. [[CrossRef](#)]
7. Irrgang, T.; Kempe, R. 3d-Metal Catalyzed N- and C-Alkylation Reactions via Borrowing Hydrogen or Hydrogen Autotransfer. *Chem. Rev.* **2019**, *119*, 2524–2549. [[CrossRef](#)]
8. Murugesan, K.; Senthamarai, T.; Chandrashekar, V.G.; Natte, K.; Kamer, P.C.J.; Beller, M.; Jagadeesh, R.V. Catalytic reductive aminations using molecular hydrogen for synthesis of different kinds of amines. *Chem. Soc. Rev.* **2020**, *49*, 6273–6328. [[CrossRef](#)]
9. Irrgang, T.; Kempe, R. Transition-Metal-Catalyzed Reductive Amination Employing Hydrogen. *Chem. Rev.* **2020**, *120*, 9583–9674. [[CrossRef](#)]
10. Dong, C.; Wu, Y.; Wang, H.; Peng, J.; Li, Y.; Samart, C.; Ding, M. Facile and Efficient Synthesis of Primary Amines via Reductive Amination over a Ni/Al₂O₃ Catalyst. *ACS Sustain. Chem. Eng.* **2021**, *9*, 7318–7327. [[CrossRef](#)]
11. Jagadeesh, R.V.; Murugesan, K.; Alshammari, A.S.; Neumann, H.; Pohl, M.-M.; Radnik, J.; Beller, M. MOF-derived cobalt nanoparticles catalyze a general synthesis of amines. *Science* **2017**, *358*, 326–332. [[CrossRef](#)] [[PubMed](#)]
12. Lator, A.; Gaillard, Q.G.; Mérel, D.S.; Lohier, J.-F.; Gaillard, S.; Poater, A.; Renaud, J.-L. Room-Temperature Chemoselective Reductive Alkylation of Amines Catalyzed by a Well-Defined Iron(II) Complex Using Hydrogen. *J. Org. Chem.* **2019**, *84*, 6813–6829. [[CrossRef](#)] [[PubMed](#)]
13. Kapnang, H.; Charles, G.; Sondengam, B.L.; Hemo, J.H. Bis (alcoyloxymethyl) amines: Preparation et reduction; N-dimethylation selective d'amines primaires. *Tetrahedron Lett.* **1977**, *18*, 3469–3472. [[CrossRef](#)]
14. Tadanier, J.; Hallas, R.; Martin, J.R.; Stanaszek, R.S. Observations relevant to the mechanism of the reductive aminations of ketones with sodium cyanoborohydride and ammonium acetate. *Tetrahedron* **1981**, *37*, 1309–1316. [[CrossRef](#)]
15. Gomez, S.; Peters, J.A.; Maschmeyer, T. The Reductive Amination of Aldehydes and Ketones and the Hydrogenation of Nitriles: Mechanistic Aspects and Selectivity Control. *Adv. Synth. Catal.* **2002**, *344*, 1037–1057. [[CrossRef](#)]
16. Yagafarov, N.Z.; Kolesnikov, P.N.; Usanov, D.L.; Novikov, V.V.; Nelyubina, Y.V.; Chusov, D. The synthesis of sterically hindered amines by a direct reductive amination of ketones. *Chem. Commun.* **2016**, *52*, 1397–1400. [[CrossRef](#)]
17. Hünig, S.; Kiessel, M. Spezifische Protonenacceptoren als Hilfsbasen bei Alkylierungs- und Dehydrohalogenierungsreaktionen. *Chem. Ber.* **1958**, *91*, 380–392. [[CrossRef](#)]
18. Step, E.N.; Turro, N.J.; Gande, M.E.; Klemchuk, P.P. Mechanism of Polymer Stabilization by Hindered-Amine Light Stabilizers (HALS). Model Investigations of the Interaction of Peroxy Radicals with HALS Amines and Amino Ethers. *Macromolecules* **1994**, *27*, 2529–2539. [[CrossRef](#)]
19. Chelucci, G. Metal-complexes of optically active amino- and imino-based pyridine ligands in asymmetric catalysis. *Coord. Chem. Rev.* **2013**, *257*, 1887–1932. [[CrossRef](#)]
20. Stephan, D.W. Frustrated Lewis pairs: From concept to catalysis. *Acc. Chem. Res.* **2015**, *48*, 306–316. [[CrossRef](#)]
21. Luo, D.; He, Y.; Yu, X.; Wang, F.; Zhao, J.; Zheng, W.; Jiao, H.; Yang, Y.; Li, Y.; Wen, X. Intrinsic mechanism of active metal dependent primary amine selectivity in the reductive amination of carbonyl compounds. *J. Catal.* **2021**, *395*, 293–301. [[CrossRef](#)]
22. Podyacheva, E.; Afanasyev, O.I.; Tsygankov, A.A.; Makarova, M.; Chusov, D. Hitchhiker's Guide to Reductive Amination. *Synthesis-Stuttgart* **2019**, *51*, 2667–2677.
23. Karageorge, G.N.; Macor, J.E. Synthesis of novel serotonergics and other N-alkylamines using simple reductive amination using catalytic hydrogenation with Pd/C. *Tetrahedron Lett.* **2011**, *52*, 5117–5119. [[CrossRef](#)]
24. Guo, M.; Jayakumar, S.; Luo, M.; Kong, X.; Li, C.; Li, H.; Chen, J.; Yang, Q. The promotion effect of pi-pi interactions in Pd NPs catalysed selective hydrogenation. *Nat. Commun.* **2022**, *13*, 1770. [[CrossRef](#)]
25. Neri, G.; Musolino, M.G.; Milone, C.; Pietropaolo, D.; Galvagno, S. Particle size effect in the catalytic hydrogenation of 2,4-dinitrotoluene over Pd/C catalysts. *Appl. Catal. A* **2001**, *208*, 307–316. [[CrossRef](#)]
26. Wang, Q.; Cheng, H.; Liu, R.; Hao, J.; Yu, Y.; Zhao, F. Influence of metal particle size on the hydrogenation of maleic anhydride over Pd/C catalysts in scCO₂. *Catal. Today* **2009**, *148*, 368–372. [[CrossRef](#)]
27. Suo, Y.; Hsing, I.M. Size-controlled synthesis and impedance-based mechanistic understanding of Pd/C nanoparticles for formic acid oxidation. *Electrochim. Acta* **2009**, *55*, 210–217. [[CrossRef](#)]

28. Li, J.; Chen, W.; Zhao, H.; Zheng, X.; Wu, L.; Pan, H.; Zhu, J.; Chen, Y.; Lu, J. Size-dependent catalytic activity over carbon-supported palladium nanoparticles in dehydrogenation of formic acid. *J. Catal.* **2017**, *352*, 371–381. [[CrossRef](#)]
29. Chinthaginjala, J.K.; Villa, A.; Su, D.S.; Mojet, B.L.; Lefferts, L. Nitrite reduction over Pd supported CNFs: Metal particle size effect on selectivity. *Catal. Today* **2012**, *183*, 119–123. [[CrossRef](#)]
30. Sun, W.; Wu, S.; Lu, Y.; Wang, Y.; Cao, Q.; Fang, W. Effective Control of Particle Size and Electron Density of Pd/C and Sn-Pd/C Nanocatalysts for Vanillin Production via Base-Free Oxidation. *ACS Catal.* **2020**, *10*, 7699–7709. [[CrossRef](#)]
31. Edwards, J.K.; Thomas, A.; Solsona, B.E.; Landon, P.; Carley, A.F.; Hutchings, G.J. Comparison of supports for the direct synthesis of hydrogen peroxide from H₂ and O₂ using Au–Pd catalysts. *Catal. Today* **2007**, *122*, 397–402. [[CrossRef](#)]
32. Xu, X.; Luo, J.; Li, L.; Zhang, D.; Wang, Y.; Li, G. Unprecedented catalytic performance in amine syntheses via Pd/g-C₃N₄ catalyst-assisted transfer hydrogenation. *Green Chem.* **2018**, *20*, 2038–2046. [[CrossRef](#)]
33. Wang, Z.; Wei, J.; Liu, G.; Zhou, Y.; Han, K.; Ye, H. G-C₃N₄-coated activated carbon-supported Pd catalysts for 4-CBA hydrogenation: Effect of nitrogen species. *Catal. Sci. Technol.* **2015**, *5*, 3926–3930. [[CrossRef](#)]
34. Wang, Y.; Yao, J.; Li, H.; Su, D.; Antonietti, M. Highly Selective Hydrogenation of Phenol and Derivatives over a Pd@Carbon Nitride Catalyst in Aqueous Media. *J. Am. Chem. Soc.* **2011**, *133*, 2362–2365. [[CrossRef](#)] [[PubMed](#)]
35. Heinen, A.W.; Peters, J.A.; Bekkum, H. The Reductive Amination of Benzaldehyde Over Pd/C Catalysts: Mechanism and Effect of Carbon Modifications on the Selectivity. *Eur. J. Org. Chem.* **2000**, *2000*, 2501–2506. [[CrossRef](#)]
36. Zhang, N.; Xie, J.; Varadan, V.K. Functionalization of carbon nanotubes by potassium permanganate assisted with phase transfer catalyst. *Smart Mater. Struct.* **2002**, *11*, 962–965. [[CrossRef](#)]
37. Carmo, M.; Linardi, M.; Rocha Poco, J.G. H₂O₂ treated carbon black as electrocatalyst support for polymer electrolyte membrane fuel cell applications. *Int. J. Hydrogen Energy* **2008**, *33*, 6289–6297. [[CrossRef](#)]
38. Li, J.; Ma, L.; Li, X.; Lu, C.; Liu, H. Effect of Nitric Acid Pretreatment on the Properties of Activated Carbon and Supported Palladium Catalysts. *Ind. Eng. Chem. Res.* **2005**, *44*, 5478–5482. [[CrossRef](#)]
39. Xu, T.-Y.; Zhang, Q.-F.; Yang, H.-F.; Li, X.-N.; Wang, J.-G. Role of Phenolic Groups in the Stabilization of Palladium Nanoparticles. *Ind. Eng. Chem. Res.* **2013**, *52*, 9783–9789. [[CrossRef](#)]
40. Song, S.; Wang, Y.Z.; Yan, N. A remarkable solvent effect on reductive amination of ketones. *Mol. Catal.* **2018**, *454*, 87–93. [[CrossRef](#)]
41. Liu, J.; Fitzgerald, A.E.; Mani, N.S. Reductive Amination by Continuous-Flow Hydrogenation: Direct and Scalable Synthesis of a Benzylpiperazine. *Synthesis-Stuttgart* **2012**, *44*, 2469–2473. [[CrossRef](#)]
42. Moro Ouma, C.N.; Modisha, P.; Bessarabov, D. Insight into the adsorption of a liquid organic hydrogen carrier, perhydro-*i*-dibenzyltoluene (*i* = *m*, *o*, *p*), on Pt, Pd and PtPd planar surfaces. *RSC Adv.* **2018**, *8*, 31895–31904. [[CrossRef](#)] [[PubMed](#)]
43. Santarossa, G.; Iannuzzi, M.; Vargas, A.; Baiker, A. Adsorption of Naphthalene and Quinoline on Pt, Pd and Rh: A DFT Study. *ChemPhysChem* **2008**, *9*, 401–413. [[CrossRef](#)] [[PubMed](#)]
44. Mittendorfer, F.; Thomazeau, C.; Raybaud, P.; Toulhoat, H. Adsorption of Unsaturated Hydrocarbons on Pd(111) and Pt(111): A DFT Study. *J. Phys. Chem. B* **2003**, *107*, 12287–12295. [[CrossRef](#)]
45. Han, M.; Wang, H.; Zhao, S.; Hu, L.; Huang, H.; Liu, Y. One-step synthesis of CoO/g-C₃N₄ composites by thermal decomposition for overall water splitting without sacrificial reagents. *Inorg. Chem. Front.* **2017**, *4*, 1691–1696. [[CrossRef](#)]
46. Qi, F.; Li, Y.; Wang, Y.; Wang, Y.; Liu, S.; Zhao, X. Ag-Doped g-C₃N₄ film electrode: Fabrication, characterization and photoelectrocatalysis property. *RSC Adv.* **2016**, *6*, 81378–81385. [[CrossRef](#)]
47. Wang, M.; Shen, S.; Li, L.; Tang, Z.; Yang, J. Effects of sacrificial reagents on photocatalytic hydrogen evolution over different photocatalysts. *J. Mater. Sci.* **2017**, *52*, 5155–5164. [[CrossRef](#)]
48. Baranova, E.A.; Le Page, Y.; Ilin, D.; Bock, C.; MacDougall, B.; Mercier, P.H.J. Size and composition for 1–5nm Ø PtRu alloy nano-particles from Cu K α X-ray patterns. *J. Alloys Compd.* **2009**, *471*, 387–394. [[CrossRef](#)]
49. Bakker, J.J.W.; Neut, A.G.v.d.; Kreutzer, M.T.; Moulijn, J.A.; Kapteijn, F. Catalyst performance changes induced by palladium phase transformation in the hydrogenation of benzonitrile. *J. Catal.* **2010**, *274*, 176–191. [[CrossRef](#)]
50. Amorim, C.; Keane, M.A. Palladium supported on structured and nonstructured carbon: A consideration of Pd particle size and the nature of reactive hydrogen. *J. Colloid Interface Sci.* **2008**, *322*, 196–208. [[CrossRef](#)]
51. Albers, P.W.; Möbus, K.; Wieland, S.D.; Parker, S.F. The fine structure of Pearlman’s catalyst. *Phys. Chem. Chem. Phys.* **2015**, *17*, 5274–5278. [[CrossRef](#)] [[PubMed](#)]
52. Jaleel, A.; Haider, A.; Nguyen, C.V.; Lee, K.R.; Choung, S.; Han, J.W.; Baek, S.-H.; Shin, C.-H.; Jung, K.-D. Structural effect of Nitrogen/Carbon on the stability of anchored Ru catalysts for CO₂ hydrogenation to formate. *Chem. Eng. J.* **2022**, *433*, 133571. [[CrossRef](#)]
53. Bulushev, D.A.; Yuranov, I.; Suvorova, E.I.; Buffat, P.A.; Kiwi-Minsker, L. Highly dispersed gold on activated carbon fibers for low-temperature CO oxidation. *J. Catal.* **2004**, *224*, 8–17. [[CrossRef](#)]
54. Das, T.K.; Banerjee, S.; Vishwanadh, B.; Joshi, R.; Sudarsan, V. On the nature of interaction between Pd nanoparticles and C₃N₄ support. *Solid State Sci.* **2018**, *83*, 70–75. [[CrossRef](#)]
55. García, G.; Silva-Chong, J.; Rodríguez, J.L.; Pastor, E. Spectroscopic elucidation of reaction pathways of acetaldehyde on platinum and palladium in acidic media. *J. Solid State Electrochem.* **2014**, *18*, 1205–1213. [[CrossRef](#)]
56. Knöpke, L.R.; Nemat, N.; Köckritz, A.; Brückner, A.; Bentrup, U. Reaction Monitoring of Heterogeneously Catalyzed Hydrogenation of Imines by Coupled ATR-FTIR, UV/Vis, and Raman Spectroscopy. *ChemCatChem* **2010**, *2*, 273–280. [[CrossRef](#)]

57. Tammer, M.G. Sokrates: Infrared and Raman characteristic group frequencies: Tables and charts. *Colloid Polym. Sci.* **2004**, *283*, 235. [[CrossRef](#)]
58. Aguirre, A.; Collins, S.E. Insight into the mechanism of acetonitrile hydrogenation in liquid phase on Pt/Al₂O₃ by ATR-FTIR. *Catal. Today* **2019**, *336*, 22–32. [[CrossRef](#)]
59. Litvak, I.; Anker, Y.; Cohen, H. On-line in situ determination of deuterium content in water via FTIR spectroscopy. *RSC Adv.* **2018**, *8*, 28472–28479. [[CrossRef](#)]
60. Raskó, J.; Kiss, J. Adsorption and surface reactions of acetonitrile on Al₂O₃-supported noble metal catalysts. *Appl. Catal. A* **2006**, *298*, 115–126. [[CrossRef](#)]
61. Wu, X.; Ge, Q.; Zhu, X. Vapor phase hydrodeoxygenation of phenolic compounds on group 10 metal-based catalysts: Reaction mechanism and product selectivity control. *Catal. Today* **2021**, *365*, 143–161. [[CrossRef](#)]
62. Ge, X.; Luo, C.; Qian, C.; Yu, Z.; Chen, X. RANEY[®] nickel-catalyzed reductive N-methylation of amines with paraformaldehyde: Theoretical and experimental study. *RSC Adv.* **2014**, *4*, 43195–43203. [[CrossRef](#)]
63. Sanyal, U.; Yuk, S.F.; Koh, K.; Lee, M.S.; Stoerzinger, K.; Zhang, D.; Meyer, L.C.; Lopez-Ruiz, J.A.; Karkamkar, A.; Holladay, J.D.; et al. Hydrogen Bonding Enhances the Electrochemical Hydrogenation of Benzaldehyde in the Aqueous Phase. *Angew. Chem. Int. Ed.* **2021**, *60*, 290–296. [[CrossRef](#)] [[PubMed](#)]
64. Brigas, A.F.; Clegg, W.; Dillon, C.J.; Fonseca, C.F.C.; Johnstone, R.A.W. Metal-assisted reactions. Part 29.1 Structure and hydrogenolysis of C–N bonds in derivatives of aromatic amines. Bond length and electronegativity changes from X-ray crystallographic data. *J. Chem. Soc. Perkin Trans. 2* **2001**, *8*, 1315–1324. [[CrossRef](#)]
65. Ong, W.-J.; Tan, L.-L.; Ng, Y.H.; Yong, S.-T.; Chai, S.-P. Graphitic Carbon Nitride (g-C₃N₄)-Based Photocatalysts for Artificial Photosynthesis and Environmental Remediation: Are We a Step Closer To Achieving Sustainability? *Chem. Rev.* **2016**, *116*, 7159–7329. [[CrossRef](#)] [[PubMed](#)]
66. Bannwarth, C.; Ehlert, S.; Grimme, S. GFN2-xTB—An Accurate and Broadly Parametrized Self-Consistent Tight-Binding Quantum Chemical Method with Multipole Electrostatics and Density-Dependent Dispersion Contributions. *J. Chem. Theory Comput.* **2019**, *15*, 1652–1671. [[CrossRef](#)]
67. Grimme, S.; Bannwarth, C.; Shushkov, P. A Robust and Accurate Tight-Binding Quantum Chemical Method for Structures, Vibrational Frequencies, and Noncovalent Interactions of Large Molecular Systems Parametrized for All spd-Block Elements (Z = 1–86). *J. Chem. Theory Comput.* **2017**, *13*, 1989–2009. [[CrossRef](#)]
68. Hratchian, H.P.; Schlegel, H.B. Using Hessian updating to increase the efficiency of a Hessian based predictor-corrector reaction path following method. *J. Chem. Theory Comput.* **2005**, *1*, 61–69. [[CrossRef](#)]
69. Truhlar, D.G.; Kilpatrick, N.J.; Garrett, B.C. Reaction-path interpolation models for variational transition-state theory. *J. Chem. Phys.* **1983**, *78*, 2438–2442. [[CrossRef](#)]
70. Fukui, K. The path of chemical-reactions—The IRC approach. *Acc. Chem. Res.* **1981**, *14*, 363–368. [[CrossRef](#)]
71. Lu, T. Gau_xtb: A Gaussian Interface for xtb Code. Available online: http://sobereva.com/soft/gau_xtb (accessed on 17 May 2021).